Journal of Aerosol Science

Flow features and micro-particle deposition in a human respiratory system during sniffing

H. Calmet[a,*], G. Houzeaux[a], M. Vázquez[a], B. Eguzkitza[a], A.M. Gambaruto[b], A.J. Bates[d], D.J. Doorly[c]

[a] Barcelona Supercomputing Center (BSC-CNS), Department of Computer Applications in Science and Engineering, Edificio Nexus II - Planta 3C/ jordi Girona, 29, 08034 Barcelona, Spain
[b] University of Bristol, Department of Mechanical Engineering, Queen's Building, University Walk, Bristol BS8 1TR, UK
[c] Imperial College London, Department of Aeronautics, Exhibition Road, London SW7 2AZ, UK
[d] Department of Pulmonary Medicine, Cincinnati Children's Hospital Medical Center, 3333 Burnet Ave, Cincinnati, OH 45229, USA

ARTICLE INFO

Keywords:
Respiratory tract
Particle transport/deposition
Computational fluid-particle dynamics

ABSTRACT

As we inhale, the air drawn through our nose undergoes successive accelerations and decelerations as it is turned, split and recombined before splitting again at the end of the trachea as it enters the bronchi. Fully describing the dynamic behaviour of the airflow and how it transports inhaled particles poses a severe challenge to computational simulations. In this paper we explore two aspects: the dynamic behaviour of airflow during a rapid inhalation (or sniff) and the transport of inhaled aerosols. The development of flow unsteadiness from a laminar state at entry to the nose through to the turbulent character of tracheal flow is resolved using accurate numerical models with high performance computing-based large scale simulations. Combining the flow solution with a Lagrangian computation reveals the effects of flow behaviour and airway geometry on the deposition of inhaled microparticles. Improved modelling of airflow and delivery of therapeutic aerosols could be applied to improve diagnosis and treatment.

1. Introduction

The sniff, a rapid and short inhalation is probably the most complex case to breathing to simulate. It involves different flow features and regimes simultaneously along the respiratory tract. The resulting airflow is composed of laminar, transitional and turbulent regimes in different airway segments. The geometry of the respiratory tract is composed of tiny passages, constriction zones and rapid changes in direction. Doorly, Taylor, Gambaruto, Schroter, and Tolley (2008) investigated variations in the nasal airways and the modelling of flow in this complex geometry, providing comparisons with numerical and experimental models (Doorly, Taylor, & Schroter, 2008). Taylor, Doorly, and Schroter (2010) demonstrated that incorporating the external nose and face reproduces the external physiological boundary conditions. Other works, such as Jayaraju, Brouns, Lacor, Belkassem, and Verbanck (2008) and Ball, Uddin, and Pollard (2008), used the human upper airway with an idealized geometry and presented results concerning mean flow and flow structures. Contrary to Jayaraju et al. (2008) and Ball et al. (2008), Ghahramani, Abouali, Emdad, and Ahmadi (2014) and Bates et al. (2017a, 2017b) used a realistic model to perform a numerical analysis in the upper human airway. Saksono, Nithiarasu, Sazonov, and Yeo (2011) and Lin, Tawhai, McLennan, and Hoffman (2007) demonstrated that incorporating the nasal cavity into the upper airway is essential in order to study the flow in the throat, since the results with and without the nasal cavity are dramatically different.

The nasal cavity is the first line of defense in the respiratory tract that filters out inhaled airborne particulate matters, thus protecting the delicate lower airways (Balásházy, Hofmann, & Heistracher, 2003). Particle deposition in human nasal cavities has been extensively studied in the past (Calmet et al., 2018; Cheng, 2003; Cheng et al., 2001, Cheng, Cheng, Yeh, and Swift, 1995; Kesavanathan and Swift, 1998; Kesavanathan, Bascom, and Swift, 1998; Kesavan, Bascom, Laube, & Swift, 2000) including nano and micro-particles, using in-vitro and in-vivo methods. However particle deposition studies based on realistic human upper airway models are less popular (Ghalati et al., 2012; Jayaraju et al., 2008). Furthermore, steady (time-constant) inhalation flow rates have also been extensively studied (Kolanjiyil & Kleinstreuer, 2013; Shi, Kleinstreuer, & Zhang, 2008b, 2007a; Zhang & Kleinstreuer, 2011). Although fewer investigations exist with unsteady inhalation flow rates, such as Bahmanzadeh, Abouali, and Ahmadi (2016) who compared micro-particle deposition under cyclic inspiratory flow with equivalent steady conditions. They concluded that while the general trend was similar, the particle deposition for equivalent steady inhalation conditions cannot accurately predict the particle deposition for cyclic inspiratory flow. To study aerosol drug delivery, unsteady particle tracking through transient (time-varying) airflow needs to be addressed in detail.

Drug delivery to the olfactory region is particularly important. This region (upper meatus below the cribiform plate) (Zhao, Scherer, Hajiloo, & Dalton, 2004) is the target of drug delivery of aerosols in the nasal cavity. The route taken by inhaled particles to reach the brain, via the olfactory pathway, is unclear. There is increasing evidence that inhaled particulate matter depositing in the olfactory region can migrate to the brain along the olfactory bulb Garcia, Schroeter, and Kimbell (2015). Due to the protected area of the human olfactory epithelium, it is estimated that only 10% of inhaled air actually reaches the olfactory region during a normal resting breath, see Hahn, Scherer, and Mozell (1993). As far as the authors know, there is no literature about micro-particle deposition in the human upper airways during sniffing.

This study aims to provide the basic information necessary to understand the flow features and the micro-particle deposition pattern happening in the human respiratory tract during sniffing. The results are presented as a journey through the human airway.

Previous studies have analyzed different aspects of the airflow with the same anatomy and boundary conditions used in this study (Bates et al., 2015; Calmet et al., 2016).

This paper is organized as follows: Section 2 presents the methods used, Section 3 presents the results of the simulation, whilst the conclusion and the discussion are presented in Section 4.

2. Methods

2.1. Geometry and mesh description

The computational domain was reconstructed from a clinically acquired computed tomography (CT) scan of a 48-year-old male subject. A consultant radiologist reported the nasal airways as clear and of normal appearance. The position of the tongue base and other soft tissues in the pharynx were deemed consistent with the patient being scanned in the supine position. The airway in the pharynx may be narrower than if the patient had been standing, but the geometry is within the normal range. Further details of the medical case are provided by Bates et al. (2015).

The surface definition was produced by semi-automatic segmentation of the medical images. This surface was then smoothed using Taubin's smoothing algorithm Taubin (1995). Further details of the segmentation are provided by Calmet et al. (2016).

An unstructured mesh was employed, due to the complex shape of the geometry, especially apparent within the intricate passageways of the nasal cavity. The mesh generation software employed was ANSYS ICEM CFD (ANSYS Inc., USA). All the meshes in this study were hybrid, made of tetrahedrons, with prism layers at the wall to resolve the boundary layer.

Three meshes were used in this study. A coarse one with 9 million elements, a fine one with 44 million elements and a very fine one with 350 million elements, see Fig. 1. In this study, particle deposition is computed only in the coarse mesh due to a relatively inefficient load balance scheme and the computational cost. We left for a future paper the required improvements to simulate particle deposition in very large meshes.

The mesh convergence study was presented previously, all the details concerning meshes and parameters are provided by Calmet et al. (2016).

2.2. Governing equation and boundary conditions

2.2.1. Fluid solver

In this section, we briefly describe the numerical method used to solve the Navier-Stokes equations: the high performance computational mechanics code Alya (Vázquez et al., 2016), which was developed at Barcelona Supercomputing Center. A deeper description of this numerical method can be found in Houzeaux and Vázquez (2008). Let μ be the viscosity of the fluid, and ρ its constant density. The problem is stated as follows: find the velocity $\boldsymbol{u}$ and mechanical pressure p in a domain Ω such that they satisfy in a time interval

$$\rho\frac{\partial \boldsymbol{u}}{\partial t} + \rho(\boldsymbol{u}\cdot\nabla)\boldsymbol{u} - \nabla\cdot[2\mu\varepsilon(\boldsymbol{u})] + \nabla p = \boldsymbol{0}, \tag{1}$$

$$\nabla\cdot\boldsymbol{u} = 0, \tag{2}$$

together with initial and boundary conditions. The velocity strain rate is $\varepsilon(\boldsymbol{u}) = \frac{1}{2}(\nabla\boldsymbol{u} + \nabla\boldsymbol{u}^t)$.

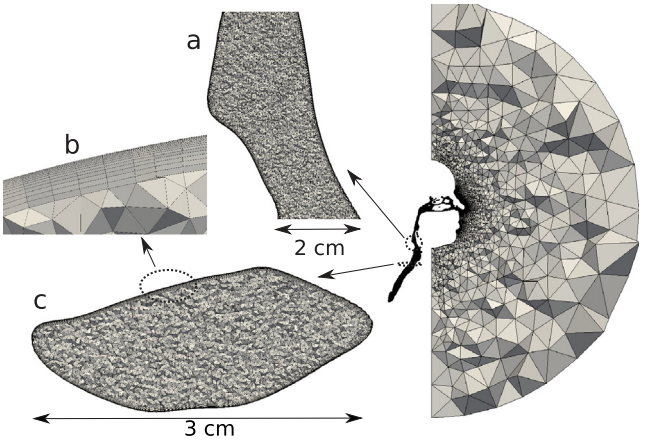

Fig. 1. Sagittal view of upper airway mesh and details: (a) section in the sagittal plane above the glottis, (b) detail of prism layers, (c) section in the axial plane in the supra-glottic region.

The numerical model of the Navier-Stokes solver is a stabilized finite element method, based on the Variational MultiScale (VMS) method (Houzeaux & Principe, 2008) which is considered an implicit Large Eddy Simulation.

The discretization of the Navier-Stokes equations yields a coupled algebraic system to be solved at each linearization step within a time loop. The resulting system is split to solve the momentum and continuity equations independently. This is achieved by applying an iterative strategy to solve for the Schur complement of the pressure. According to our scheme, at each linearization step it is necessary to solve the momentum and continuity equation twice. This split strategy is described and validated in Houzeaux, Aubry, and Vázquez (2011).

The Alya code is written in Fortran90/95 and parallelized with MPI. The partition of the mesh is carried out on-the-fly with the METIS library (Karypis, 1995).

As shown in Figs. 1 and 2, the computational area of this study begins on the exterior of the subject's face and continues through the bilateral nasal passages, through the pharynx, larynx, trachea and finally down to the third branch generation of the bronchi. A no-slip boundary condition is imposed on the passage walls and the flat surface of the external hemisphere.

2.2.2. Micro-particle transport

Particle and fluid transport are solved simultaneously in Alya. The parallelization scheme for particle transport is radically different than that of the fluid, which can lead to an important miss-balance. Houzeaux et al. (2016) described both the implementation method and the strategy to avoid bottlenecks.

The transport of particles is simulated in a Lagrangian frame of reference, following each particle individually. From the numerical point of view, the main assumptions to develop the model are:

- Particles are assumed sufficiently small to neglect their effect on the air: therefore, a one way coupling is considered;

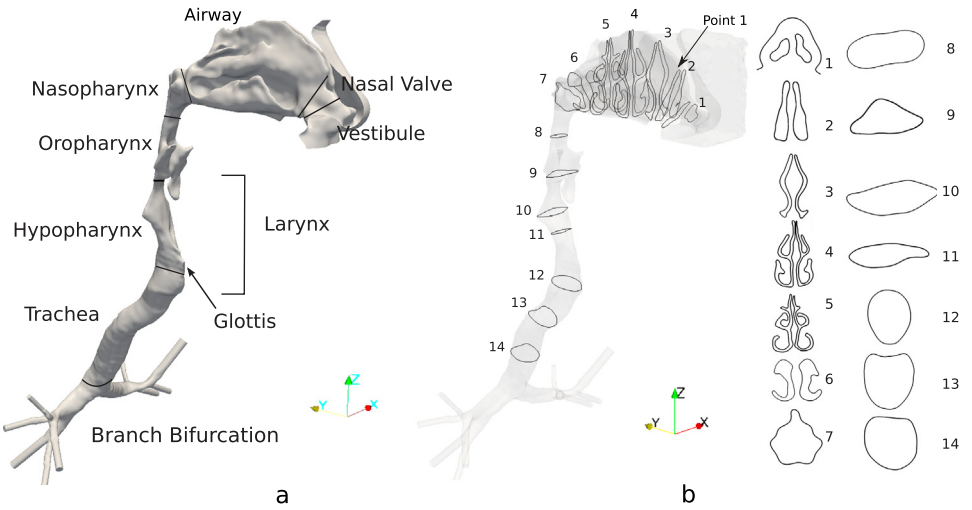

Fig. 2. (a) Nomenclature of the approximate regions of the upper airways. (b) Location of different slices and point along the airways.

- Particles do not interact with each other;
- Particle rotation is neglected;
- Thermophoretic forces are neglected;
- The forces considered are: drag F_d, gravitational and buoyancy F_g;

Let x_p, u_p, a_p be the dynamical variables of particle p, namely the position, velocity and acceleration, respectively. Let m_p be its mass, ρ_p its density, d_p its diameter, and V_p its volume. Particles are transported solving Newton's second law, and by applying the series of forces mentioned previously:

$$a_p = (F_d + F_g)/m_p. \tag{3}$$

The equation for the drag force assumes the particle has reached its terminal velocity and is given by

$$F_d = -\frac{\pi}{8}\mu d_p C_d \,\mathrm{Re}(u_p - u_f), \tag{4}$$

where Re is the particle Reynolds number based on its relative velocity with the fluid:

$$\mathrm{Re} = \frac{|u_p - u_f| d_p}{\nu}.$$

The drag coefficient is given by Ganser's formula Ganser (1993):

$$Cd = \frac{24}{\mathrm{Re}\, k_1}(1 + 0.1118(\mathrm{Re}\, k_1 k_2)^{0.6567}) + 0.4305\frac{k_2}{1 + 3305/(\mathrm{Re}\, k_1 k_2)},$$
$$k1 = \frac{3}{1 + 2\psi^{-0.5}},$$
$$k2 = 10^{1.84148(-\log_{10}(\psi))^{0.5743}},$$
$$\psi = \text{sphericity, (=1for a sphere).}$$

The gravity and buoyancy forces contribute to the dynamics of the particle whenever there is a difference in densities:

$$F_g = V_p g(\rho_p - \rho),$$

with g being the gravity vector.

Inflow condition. The inflow velocity is imposed as a Dirichlet condition on the hemisphere dome. It is prescribed as a time varying uniform velocity with direction normal to the hemisphere. To model the sniff, we use a polynomial function of order 10 derived from the experimental work detailed in Rennie et al. (2011), in which several short inhalations from rest were measured for different subjects. The 10^{th} order polynomial function (see Eq. (5)) describing the temporal evolution of the flow rate is provided in Fig. 3, with the coefficients of the flow defining Eq. (5) referenced in the appendix.

$$P(t) = \sum_{i=0}^{10} C_i t^i \times 1.74 \tag{5}$$

Particle injectors were located at each nostril at slice 1, see Fig. 2 and particles were distributed uniformly at the slice. Four different particle sizes, i.e., $d_p = 1$, 5, 10, 20 μm were considered. 12,500 particles for each size were released at the initial time and re-injected every 0.05 s until the last injection time (0.45 s) thus a total of 9 times during the sniff period. The total number of released particles during the entire simulation was 450,000. 20,000 suspended particles were present in the domain at the end of the

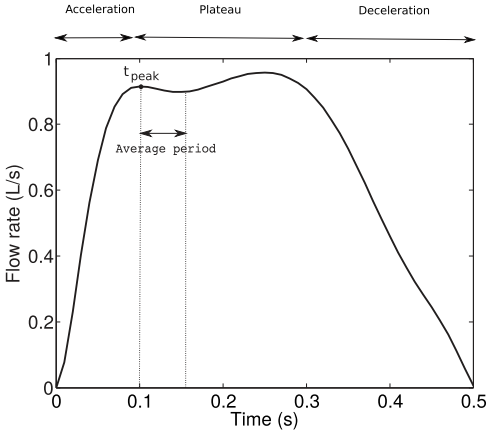

Fig. 3. Flow rate profiles and average period, The 10^{th} order polynomial function is given in the appendix see Eq. (5) and Table 1.

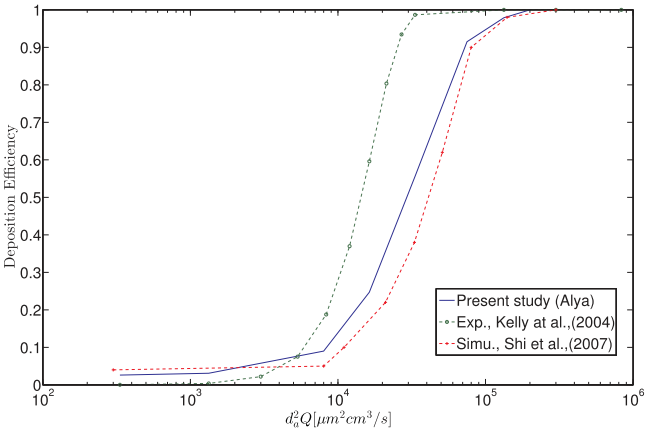

Fig. 4. Particle deposition efficiency comparison between simulations and experiment.

simulation, which represents less than 1% of the relative error for each particle size considering the total deposition result. The initial velocities of particles were assumed to be the same as the airflow velocity at the nostril. Once the particle have crossed an outlet boundary element, the particle is out of the computational domain and removed from the simulation. Furthermore particles are deposited as soon as they get in contact with wall boundaries.

We consider deposition efficiency as the ratio of particles deposited on a given surface with respect to the number of injected particles. Based on previous studies (Ghalati et al., 2012; Shi, Kleinstreuer, & Zhang, 2007b) and convergence tests, the number of particles of each size released at each time (12,500) is above the number necessary to ensure deposition results which are independent of the number released.

Outflow condition. A zero-traction outflow condition is imposed as a Neumann condition (the surface is free from external stress) at the third bronchial branch. In order to ensure fully developed flow at the outflow sections, the final bronchial branches were extruded to constant cross-sectional pipes for several diameters. These bronchial branches are set to have the 5 last layers of elements with higher constant viscosity to reduce turbulence and thus to avoid entrant flow that would unstabilize the solution.

2.3. Micro-particle deposition validation

Micro-particle deposition in the nasal cavity was compared to the experimental data reported by Kelly, Asgharian, Kimbell, and Wong (2004) as depicted in Fig. 4. The experimental data is based on results with smooth walls and their human nasal cast is based on the same MRI file as employed for the present validation. Furthermore, other numerical results Shi et al. (2007b) are plotted with Shi et al., (2007) labeled on Fig. 4.

In order to provide reproducibility and clarity of results, the impaction parameter (IP) is introduced and can be expressed as:

$$IP = d_a^2 \cdot Q \tag{6}$$

where d_a is the particle aerodynamic diameter and Q is the volumetric airflow rate. The aerodynamic diameter is that of a sphere with unit density ($1\ g/cm^3$) and its mass is equal to the mass of the actual particle.

The particle deposition efficiency is defined as:

$$\eta = \frac{N_{dep}}{N_{in}} \tag{7}$$

where N_{dep} is the number of particles deposited on the surface area of interest, which can be the total respiratory tract wall or local surface areas, e.g., olfactory regions, and N_{in} is the total number of particles released at the nostrils.

3. Results

Flow features occurring in the nasal cavity and the throat during the sniff are described in the following section. Then analysis of the particle deposition map with total and regional deposition efficiencies is presented.

3.1. Airflow

The sniff flow profile is short, transient and unsteady. It can be divided into three phases: the acceleration [0–0.1 s], the plateau [0.1–0.3 s] and the deceleration [0.3–0.5 s]. Each phase results in a distinct flow field, largely due to the resulting forces driving the inspiration. The plateau phase is the most appropriate segment of the flow profile for the turbulence analysis as the velocity is approximately constant, and the time window is of sufficient duration to calculate turbulence statistics.

A time window during the plateau phase of [0.1–0.15 s] is chosen to compute the mean flow and the turbulence measures. This

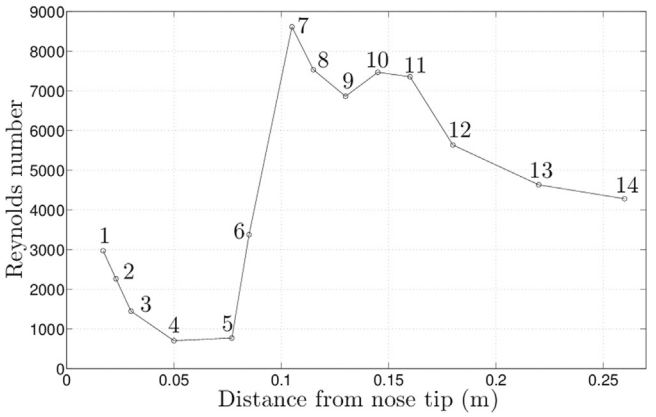

Fig. 5. Cross-sectional-area-average Reynolds number as a function of distance from nose tip. The number positions refer to the different slices see Fig. 2.

window was chosen as it is sufficiently long enough due to the fine temporal resolution available, and sufficiently short to avoid large-scale transients interfering with the analysis. The time at which the instantaneous flow field is shown is $t_{peak} = 0.1\ s$ because the bulk flow field is considered established (Doorly, Taylor, Gambaruto et al., 2008).

In order to capture the unsteadiness of airflow features, results are presented in the following section (Section 3.1) are produced with the fine mesh, i.e: 44 million elements, 0.3 mm grid size and time step of 1. $10^{-5}s$, see Calmet et al. (2016).

3.1.1. Laminar to transitional flow in nasal cavity

Monitoring the local Reynolds number along the tract gives information on the flow regime. The local Reynolds number was calculated based on the area-average velocity and hydraulic diameter of each slice as previously defined Shi, Kleinstreuer, & Zhang (2008a). The flow rate used to compute the Reynolds number was the peak value of the sniff function, $Q_{peak} = 0.9Ls^{-1}$ corresponding to $t_{peak} = 0.1\ s$, see Fig. 5.

To determine if the flow is laminar, transitional or turbulent, the value of the local Reynolds number is not sufficient, in complex geometry and/or complex inflow conditions, additional information is needed. A detailed analysis of the spectra is required to state the character of the flow: laminar/transitional/turbulent.

The Reynolds numbers at the first slices close to the nasal valve (slices 1 and 2) are between the laminar and turbulent regimes, which indicates a possible transitional flow. While the values at slices crossing the turbinate region (slices 3, 4, and 5) indicate possible laminar flow.

The transitional regime can be observed in one of two ways; one is the visual analysis of the temporal evolution of the flow (Doorly et al., 2008), another is Fourier analysis of local velocity spectra with time, which produces some clear harmonic peaks in the low frequency ranges (Sumer & Fredsøe, 2006). Calmet et al. (2016) demonstrated that the flow in the nasal cavity is unsteady downstream of the nasal valve. A key feature of this unsteady flow is the vortex shedding and flapping motion of the shear layer, located on the boundary between the nasal valve jet and the superior separated flow region. Spectral analysis of these large-scale motions can provide relevant information.

A one-dimensional spectral analysis of all components of the fluctuation in velocity is computed for the time period [0.1–0.15 s], (the start of the plateau phase of the sniff waveform). All the details concerning the spectral analysis and parameters are provided by Calmet et al. (2016).

Fig. 6 is the normalized energy spectrum of local velocity fluctuations at point 1 (see Fig. 2), located within the right nasal cavity and a closer view of the zone of interest, where the harmonic peaks are observed. These peaks correspond to those noted previously, both numerically by Calmet et al. (2016), and experimentally by Doorly et al. (2008), indicating transitional flow at this point.

Further downstream of the nasal valve, the values of the local Reynolds number (slices 3, 4, and 5) show a laminar regime along the nasal turbinate region. This tendency was also observed in this region by Shi et al. (2008a).

The flow entering the nostril changes direction drastically in the nasal valve, going from vertical to horizontal as the flow passes through the constriction of the nasal valve. This complex geometry produces some specific features and unsteady phenomena, see Fig. 6. Then, most of the inhaled air flows through the wider middle-to-low portion of the main nasal passageway, which is free of obstacles.

At the rear of the nasal cavity, the septum ends, allowing the left and right nasal cavities join in the nasopharynx.

3.1.2. Transitional to turbulent flow in the nasopharynx

The nasopharynx is a region where the confluence of the different outflow velocities from the left and right cavities mix together. Fig. 7 shows the complexity of this particular flow, where two different airflows join in a region of significant curvature.

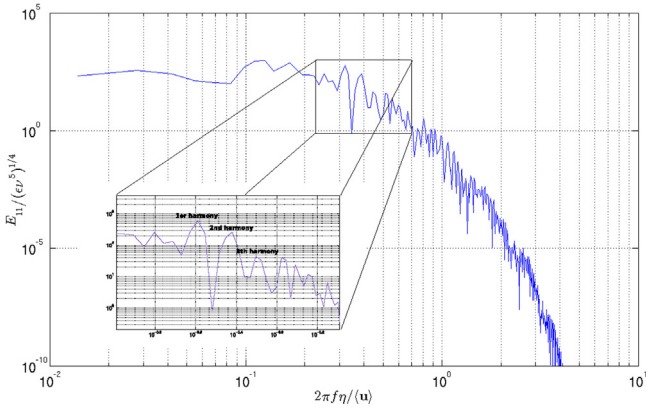

Fig. 6. Normalized energy spectrum of velocity fluctuations at the location point 1, see Fig. 2 and (inset) detailed view of the zone of interest.

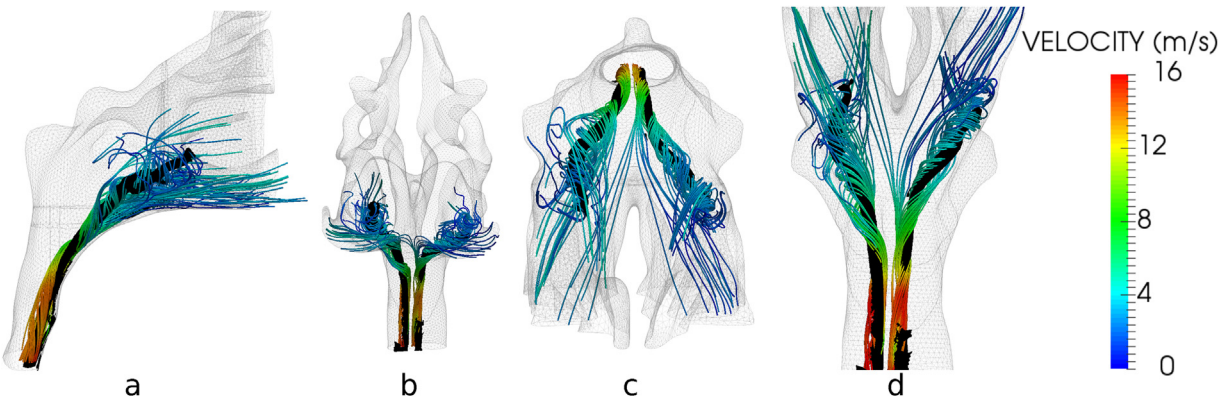

Fig. 7. Streamlines colored by velocity magnitude and black iso-surface of Q-criterion of different views of the nasopharynx at $t_{peak} = 0.1$ s (a) Lateral view. (b) Front view. (c) Top view. (d) Down isometric view.

Fig. 7 shows streamlines colored by velocity magnitude and iso-surfaces of Q-criterion in different views of the nasopharynx at $t_{peak} = 0.1$ s. Here Q-criterion is used to perform vortex identification as defined by Hunt (1987).

$$Q = \frac{1}{2}(\| \bar{\Omega} \|^2 - \| \bar{S} \|^2) > 0 \tag{8}$$

where, S and Ω are, respectively, the symmetric (strain and shear) and antisymmetric (rotation) components of the velocity gradient. When the Q-criterion is positive, it represents locations in the flow where the rotation Ω dominates the strain and shear S. Dean vortices (Ligrani & Niver, 1988) are observed, resulting from the curved passage undergoing an almost 90 ° bend from the horizontal nasal passage to the vertical descending sections. Only two main symmetric swirling vortices are represented, although the flow in the nasopharynx is more complex than these two vortical structures.

These two symmetric swirling vortices are located at the inferior part of the nasopharynx, called the soft palate, the symmetric locations and their strengths are identical. Further down, the velocity jumps by a factor of 4 at the end of nasopharynx due to sharp cross-sectional area reduction in the passage. Furthermore, the presence of Dean vortices can include events leading to transition to turbulent flow (Ligrani & Niver, 1988).

The value of the local Reynolds number for slice 6 in Fig. 5 indicates possible transitional flow while the values for slices 7 and 8 are turbulent. Wilcox defined the turbulence intensity as a turbulence indicator for internal flow (Wilcox et al., 1998),

$$I_{turb} = \sqrt{\frac{2TKE}{3U^2}} \tag{9}$$

where TKE is the turbulence kinetic energy and U is the area-average velocity. Fig. 8 shows the Cross-sectional-area-average of turbulence intensity calculated with the area-average of TKE and the area-average velocity of each slice during the plateau phase of [0.1–0.15 s], see Fig. 2.

In the nasopharynx section (slice 7 and 8), the turbulence intensity is above 7%, describing transitional-turbulent flow. This can be observed in the appendix section where the cross sections of TKE are displayed (see Fig. 13). High values are observed for the slices 7 and 8.

Fig. 8 shows that the turbulence intensity in the nasal cavity (slices 1–6) is unexpectedly high, between 5% and 10%. While these

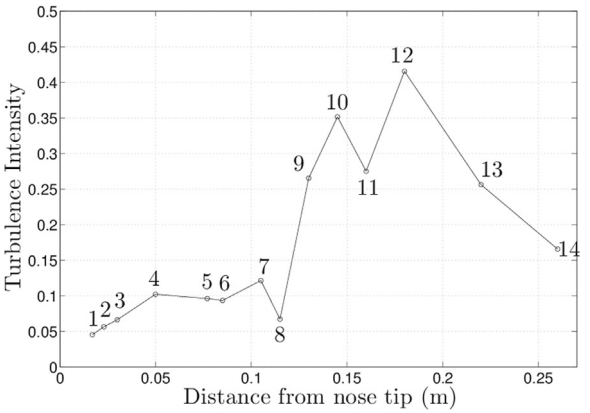

Fig. 8. Cross-sectional-area-average turbulence intensity as a function of distance from nose tip. The number positions refer to the different slices described in Fig. 2.

values would suggest turbulence in this region, the values are not caused by turbulent flow, but by the high values of Reynolds stresses, produced by unsteady flow oscillations in the nasal cavity where the complex geometry here promotes unsteady flow. In Section 3.1.1, it was demonstrated than the flow in the nasal cavity is laminar-transitional but not turbulent. Therefore, in Fig. 13, low values of *TKE* in the nasal cavity are observed.

Due to the high level of fluctuations produced by the laryngeal jet (Bates et al., 2015; Calmet et al., 2016), the flow in the laryngeal section (the throat) is clearly turbulent, see Fig. 8, with 2 peaks (slice 10 and 12).

3.1.3. Turbulent flow in the laryngeal region

Fig. 9 qualitatively illustrates the location of the vortical structures in the pharyngolaryngeal region. There is a transition of the vortical structures' direction, initially tangentially aligned with the flow direction in the nasopharynx region, while further downstream in the larynx, the flow turbulence has undergone a cascade from larger to smaller structures which are now aligned largely transversally to the flow direction. The vortices aligned with the flow direction in the nasopharynx, Dean vortices, are described in Section 3.1.2.

From Fig. 9 we can visually identify the source of instabilities and the production of turbulence structures. At the nasopharynx there is a severe stenosis that forms a jet with longitudinal vortical structures, which enters the oropharynx where there is a sudden expansion in the cross-sectional area of the passage. The fluid mechanics behaviour of free jets is that of Kelvin-Helmholtz instability, which occurs when there is a velocity difference across the interface between the higher velocity jet and the surrounding air into which it discharges. These instabilities promote a cascade from large vortex structures to smaller ones, resulting in a turbulent flow, see Fig. 8, slice 10. Again we observe a second stenosis in the downstream section of the oropharynx due to the subject lying in supine

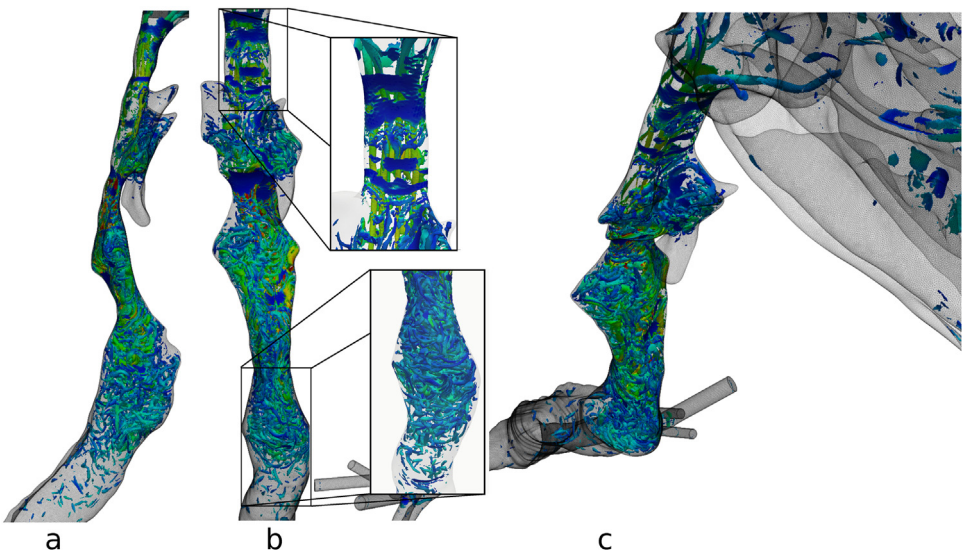

Fig. 9. Iso-surface of the Q-criterion (value$=4.5 \times 10^5$), colored by the angular velocity, in the pharyngolaryngeal region at $t_{peak} = 0.1\ s$. (a) Lateral view. (b) Front view. (c) Isometric view.

position and the tongue relaxing, reducing the patency of the passage. After this stenosis there is again a change in anatomy that promotes gradients across shear layers and the production of turbulence, see Fig. 8, slice 12. As the flow moves downstream, by the time it reaches the trachea the turbulence structures have largely broken down and dissipated, matching behaviour previously described Bates et al. (2016a, 2016b, 2017a, 2017b).

3.2. Micro-particle deposition

In this section the results of the particle deposition during sniffing are presented, first for each size of particles injected, i.e., 1, 5, 10 and 20 μm, then sorted with the three different phases of the sniff, i.e., acceleration, plateau and deceleration, see Fig. 3. Then the particle deposition efficiency, defined in Eq. (7), in the olfactory cleft for all the injected particle sizes are shown.

All results presented in this section (Section 3.2) were obtained with the coarse mesh, i.e; 9 million elements, 0.5 mm size of volume element and time step of 1. 10^{-4} s. The motivation of using the coarse mesh and the bigger time step was due to computational cost and a relatively inefficient load balance scheme. It is very computationally expensive to simulate unsteady particle tracking with a fine mesh and time step. Then we assumed that the unsteadiness aspect of the airflow is weak in the nasal cavity thus the inertial deposition mechanism is relatively unaffected. Therefore the turbulent state in the laryngeal region is captured with both meshes.

Fig. 10 shows the deposition pattern for each particle size injected in the realistic geometry of the human upper airway system during sniffing. η_{nasal} represents the nasal cavity deposition efficiency and d_p the size of the particle diameter. The regional deposition fraction is calculated according to the nomenclature defined in Fig. 2.

Clearly, the main physical mechanism of deposition in action at this range of particle size during sniffing is the inertial impaction, which is proportional to the airflow rate and the particle diameter squared, as expressed with the impaction parameter in Eq. (6).

η_{nasal} increases when particle diameter size increases, until almost 100% for the particle with an aerodynamic diameter of 20 μm. As a consequence of their higher inertia and deviation from the flow streamlines, larger particles (10 and 20 μm) stay trapped in the nasal cavity playing the role of filter. Smaller particles (1 and 5 μm) with low inertia can penetrate further. These smaller particles have the tendency to be deposited more uniformly along the respiratory tract than larger particles, even until the lungs. Some local prominent accumulation of deposited particles (hot spots) are located in the nasal cavity, the nasopharynx and finally in the larynx. A greater analysis of the zonal deposition in the nasal cavity will be the scope of subsequent investigation.

The hot spot observed in the nasopharynx is produced by the centrifugal force occurring in the 90 ° bend passageway acting on the particles. The other hot spot is located in the laryngeal region. In Section 3.1.3 it was demonstrated that the level of turbulence intensity is highest in the larynx during sniffing. This chaotic flow promotes particle deposition through turbulence dispersion.

Fig. 11 shows the deposition pattern for all the injected particle sizes under the three different phases of the sniff (Fig. 3) and the corresponding regional deposition fraction.

Acceleration phase. The inlet flow rate increases suddenly from zero to $1L/s$ in 0.1 s. This short and rapid acceleration produces implications for the deposition. As mentioned previously in this section, the main physical mechanism of deposition in this study is inertial impaction. The deposition efficiency increases with both increasing flow rate and particle diameters. The pattern of deposition shows that lager particles (green and blue spheres) are located in the nasal cavity. The higher inertia and deviation from the flow streamlines of larger particles during acceleration significantly effects the deposition. On the contrary, deposition of smaller particles (red and orange spheres) are scattered along the respiratory tract, particularly in the laryngeal region.

Plateau phase. During this phase, the flow rate is approximately constant during for 0.2 s. The deposition fractions are almost equivalent for lager particles and are located exclusively in the nasal cavity. As during the acceleration phase, the deposition fraction for smaller particles are scattered along the respiratory tract with a higher value in the hypopharynx for 1 μm particle size and the nasal cavity for 5 μm particle size. It is noticeable that the regional deposition fraction for the plateau condition is proportional to that for the entire duration of the sniff, see Fig. 10. Therefore, the particle deposition would be similar in a transient simulation of a sniff and an equivalent steady inhalation condition. This hypothesis would help to reduce the computational cost of the simulation. This assumption has to be verified and will be the scope of subsequent investigation.

Deceleration phase. The values of particle deposition during the period of the deceleration are the lowest of the three phases. The deposition pattern is very similar to that from the acceleration period.

Fig. 12 shows the particle deposition efficiency in the olfactory cleft for all the injected particle sizes over the course of the sniff. As expected, the values of η are low, as the olfactory cleft region is a protected zone in the nasal cavity, see Section 3.1.1. The deposition efficiency of the 10 μm particle size is remarkably high, 2.7%. Even the 20 μm particle size has relatively high deposition with 0.5%. Garcia et al. (2015) compared the olfactory deposition of inhaled nano-particles in humans and rats and they commentated that the highest value was $\eta = 1\%$, although that study had a constant flow rate lower than that used here, and investigated nano-particles. The result that $\eta = 2.7\%$ for 10 μm particle size represents a high deposition of particles in the olfactory cleft, the target region for many therapeutic aerosols. However, olfactory deposition is expected to vary among individuals (Garcia et al., 2015) and more investigation is required to confirm these results.

4. Conclusion

The purpose of this study was to explore and describe the features of unsteady flow occurring in the upper and descending airways and micro-particle deposition occurring during a rapid and short inhalation. The chosen inspiratory waveform is of interest as an extreme case of strong forced breathing, leading to complex fluid mechanics, and is often associated with methods of drug delivery or other behaviours, for example short repeated sniffing is a common inspiration waveform used to smell objects.

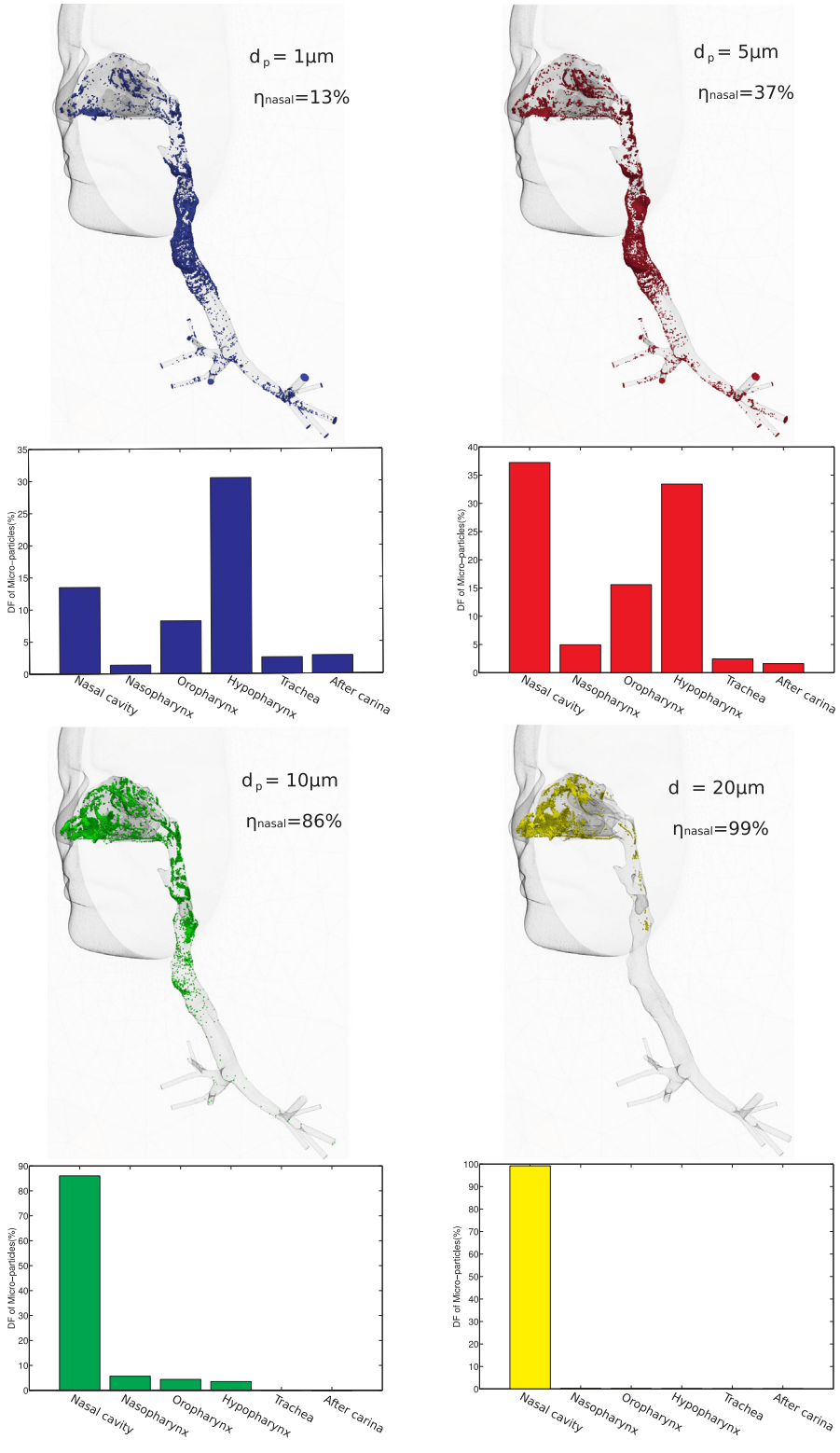

Fig. 10. Deposition patterns and regional deposition fraction for 1, 5, 10 and 20 μm during the sniff.

Thanks to the use of a simulation code specially designed for large-scale computational resources, the numerical model presented was able to simulate all the flow regimes across the different regions of the airway. Spectral analysis showed the flow regime in the nasal cavity to be laminar to transitional. Analysis of the airflow within the nasal cavity gives highlights many intricacies of this wall-

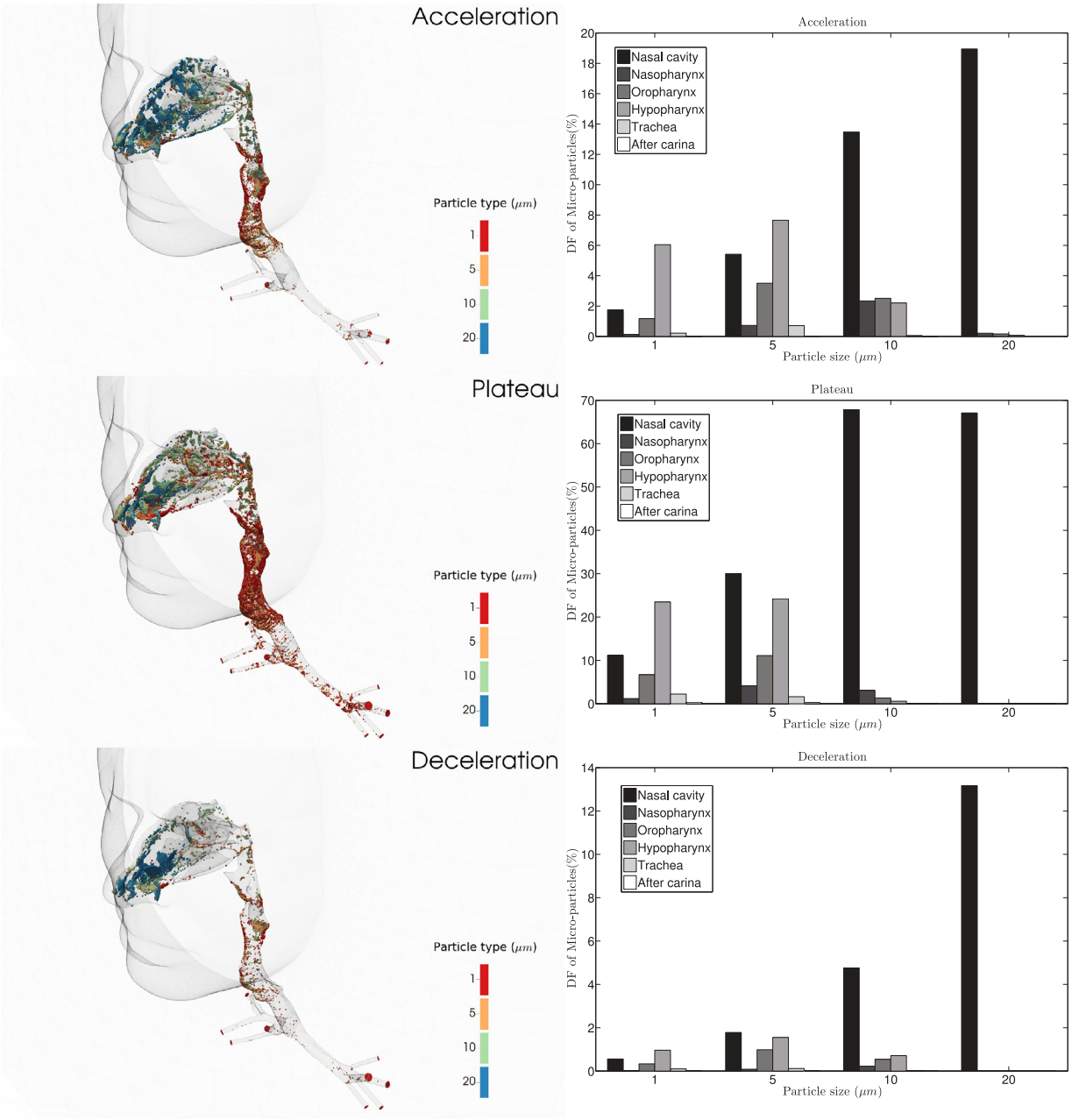

Fig. 11. Deposition patterns and regional deposition fraction for the three phases of the sniff: acceleration, plateau and deceleration, see Fig. 3.

bounded flow. These include the flow partitioning, which is effected by the nasal valve directing the flow far upstream as a jet, and the turbinate structures that project into the passages and divide the airspace, diverting the airflow to different regions of the cavity.

The main flow features present in the nasopharynx are highlighted, and the transitional to turbulent flow regime happening in this region is discussed. The turbulent flow in the laryngeal region is described, illustrated by the complex configuration of vortical structures. This is the dominant site of turbulence production, more precisely located in the supra-glottic region. As the flow reaches the lower portion of the trachea, the turbulence intensity is greatly reduced, with few vortical structures identifiable.

Modelling of micro-particle deposition in a realistic human upper airway geometry during sniffing demonstrated that the most important deposition mechanism is inertial impaction. As a consequence of their higher inertia and deviation from the flow streamlines, larger particles (10 and 20 μm) stay trapped in the nasal cavity which plays the role of filter. Smaller particles (1 and 5 μm) with low inertia can penetrate further. These smaller particles have the tendency to be deposited more uniformly than larger particles along the respiratory tract even reaching the lungs. Some hot spots are observed, of which the most important is the laryngeal region, where chaotic flow highly promotes particle deposition.

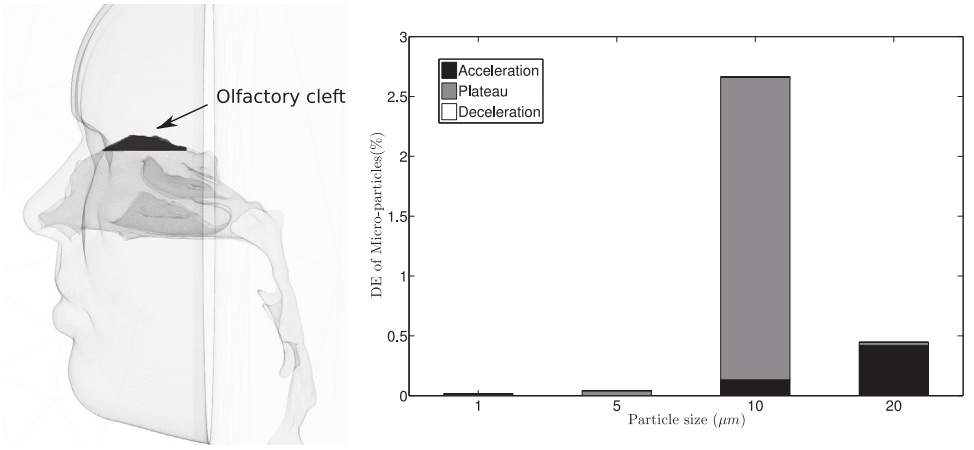

Fig. 12. Location of olfactory cleft and deposition efficiency for 1, 5, 10 and 20 μm under sniff condition.

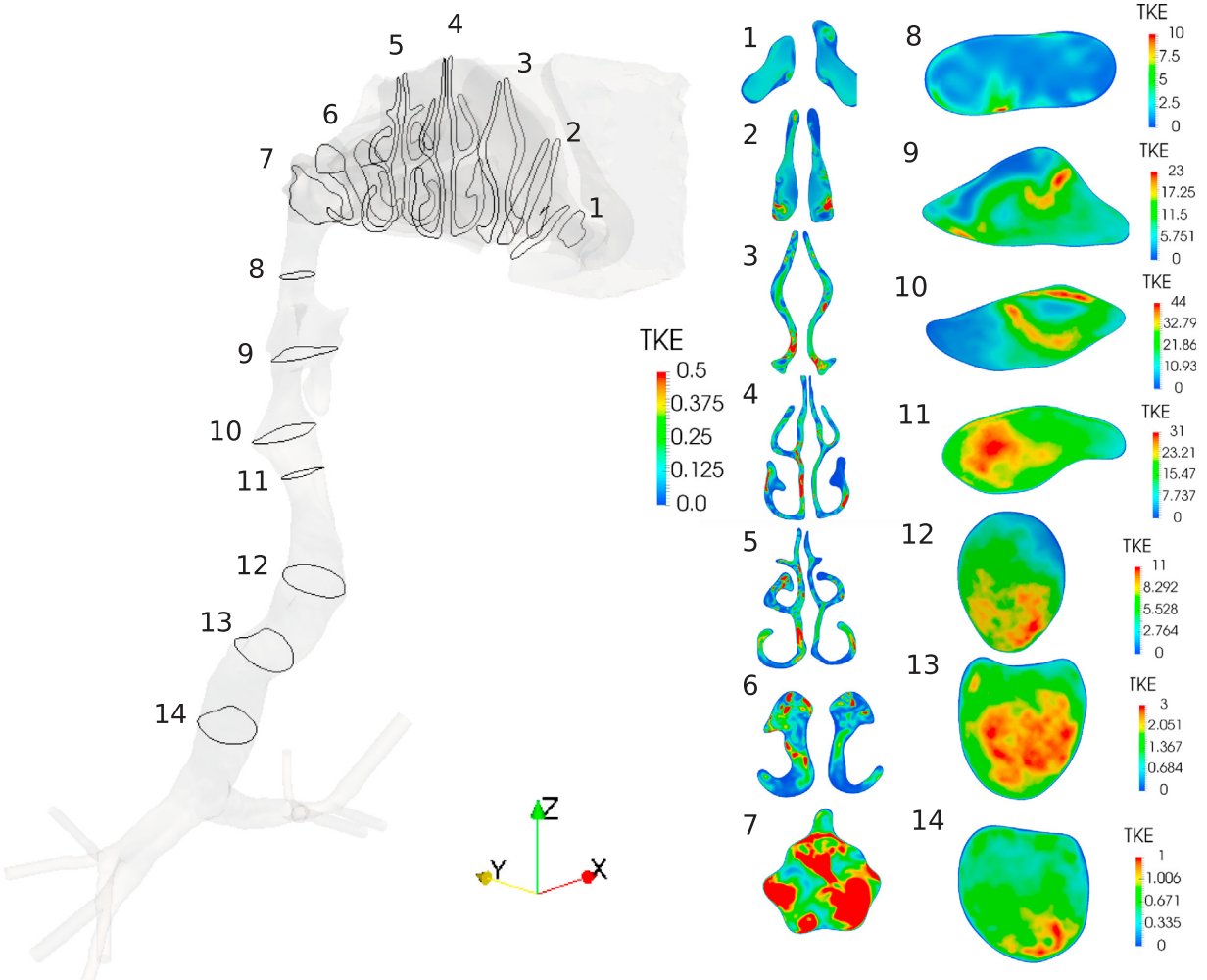

Fig. 13. Cross-sectional-area-average of TKE (m^2/s^2) along the airway during the plateau phase of [0.1–0.15 s].

The regional deposition fraction is almost identical during just the duration of the flow plateau as during the entire sniff duration. Furthermore, the highest deposition efficiency in the olfactory region is $\eta = 2.7\%$ for 10 μm particle size, which could represent a significant dose for therapeutic aerosols. This finding will be investigated further in future investigations with finer mesh density and a smaller time step.

Due to the posture of the subject, the production of turbulence in the supra-glottic region, and its intensity, may be considerably altered if the subject were in the upright position, for example as the tongue would not relax into the airspace. Further investigation of the anatomic geometry in different postures will be beneficial, as well as analysis of further subject specific cases. The study has considered a specific waveform, namely a sniff profile taken as from population average, and it will be valuable to explore the fluid mechanics for different breathing patterns.

Identical micro-particle deposition under the sniff condition and equivalent steady inhalation condition has to be investigated. This hypothesis would be helpful to reduce the computational cost of the simulation. This assumption has to be verified in future investigations.

The olfactory region is still a challenging target for drug delivery in the respiratory airways. The effects of inter- and intra-subject-variability in terms of both inhalation dynamics and anatomy need further investigation to confirm the trend found in this study across the wider population.

Acknowledgements

We acknowledge PRACE for awarding us access to the FERMI resource based in Italy at Bologna hosted by Cineca. This work was financially supported by the PRACE project Pra04 693. (2011050693 to the Fourth PRACE regular call).

Appendix

Modelling of the sniff. To model the inflow boundary condition representing a sniff, we use a polynomial function of order 10 derived from the experimental work detailed in Rennie et al. (2011). The 10^{th} order polynomial function describing the temporal evolution of the flow rate is provided in Fig. 3 (Table 1).

Table 1
Coefficient values of the 10^{th} order polynomial function.

Order	Coefficient
0	0.0015
1	0.6813
2	472.2648
3	− 10,790.8421
4	114269.4525
5	705483.2425
6	2736179.6777
7	− 6,773,661.0554
8	10395525.1742
9	− 9,007,136.2292
10	3,364,786.7418

TKE along the upper airway. *TKE* is calculated with the area-average of *TKE* of each slice during the plateau phase of [0.1–0.15 s]. The scale of *TKE* for the nasal cavity are low (less than 0.5). In contrary for the rest of the upper airway, the values of *TKE* are significantly high, emphasizing the transitional-turbulent state of the airflow.

References

Bahmanzadeh, H., Abouali, O., & Ahmadi, G. (2016). Unsteady particle tracking of micro-particle deposition in the human nasal cavity under cyclic inspiratory flow. *Journal of Aerosol Science, 101*, 86–103.

Balásházy, I., Hofmann, W., & Heistracher, T. (2003). Local particle deposition patterns may play a key role in the development of lung cancer. *Journal of Applied Physiology, 94*, 1719–1725.

Ball, C. G., Uddin, M., & Pollard, A. (2008). Mean flow structures inside the human upper airway. *Flowing, Turbulence and Combustion, 81*, 155–188.

Bates, A. J., Cetto, R., Doorly, D. J., Schroter, R. C., Tolley, N. S., & Comerford, A. (2016b). The effects of curvature and constriction on airflow and energy loss in pathological tracheas. *Respiratory Physiology and Neurobiology, 234*, 69–78.

Bates, A. J., Comerford, A., Cetto, R., Doorly, D. J., Schroter, R. C., & Tolley, N. S. (2017). Computational fluid dynamics benchmark dataset of airflow in tracheas. *Data in Briefing, 10*, 101–107.

Bates, A. J., Comerford, A., Cetto, R., Schroter, R. C., Tolley, N. S., & Doorly, D. J. (2016a). Power loss mechanisms in pathological tracheas. *Journal of Biomechanics, 49*, 2187–2192.

Bates, A. J., Doorly, D. J., Cetto, R., Calmet, H., Gambaruto, A. M., Tolley, N. S., et al. (2015). Dynamics of airflow in a short inhalation. *Journal of Royal Society Interface.*

Bates, A. J., Schuh, A., Amine-Eddine, G., McConnell, K., Loew, W., Fleck, R. J., et al. (2017a). Assessing the relationship between movement and airflow in the upper airway using computational fluid dynamics with motion determined from magnetic resonance imaging. *Clinical Biomechanics, 0*.

Calmet, H., Gambaruto, A. M., Bates, A. J., Vázquez, M., Houzeaux, G., & Doorly, D. J. (2016). Large-scale cfd simulations of the transitional and turbulent regime for the large human airways during rapid inhalation. *Computers in Biology and Medicine, 69*, 166–180.

Calmet, H., Kleinstreuer, C., Houzeaux, G., Kolanjiyil, A., Lehmkuhl, O., Olivares, E., et al. (2018). Subject-variability effects on micron particle deposition in human nasal cavities. *Journal of Aerosol Science, 115*, 12–28.

Cheng, K. H., Cheng, Y. S., Yeh, H. C., & Swift, D. L. (1995). Deposition of ultrafine aerosols in the head airways during natural breathing and during simulated breath holding using replicate human upper airway casts. *Aerosol Science and Technology, 23*, 465–474.

Cheng, Y. S. (2003). Aerosol deposition in the extrathoracic region. *Aerosol Science & Technology, 37*, 659–671.

Cheng, Y. S., Holmes, T. D., Gao, J., Guilmette, R. A., Li, S., Surakitbanharn, Y., et al. (2001). Characterization of nasal spray pumps and deposition pattern in a replica of the human nasal airway. *Journal of Aerosol Medicine, 14*, 267–280.

Doorly, D. J., Taylor, D. J., Gambaruto, A. M., Schroter, R. C., & Tolley, N. (2008a). Nasal architecture: Form and flow. *Philosophical Transactions of the Royal Society A, 366*, 3225–3246.

Doorly, D. J., Taylor, D. J., & Schroter, R. C. (2008b). Mechanics of airflow in the human nasal airways. *Respiratory Physiology & Neurobiology, 163*, 100–110.

Ganser, G. (1993). A rational approach to drag prediction of spherical and nonspherical particles. *Powder Technology, 77*, 143–152.

Garcia, G. J., Schroeter, J. D., & Kimbell, J. S. (2015). Olfactory deposition of inhaled nanoparticles in humans. *Inhalation Toxicology, 27*, 394–403.

Ghahramani, E., Abouali, O., Emdad, H., & Ahmadi, G. (2014). Numerical analysis of stochastic dispersion of micro-particles in turbulent flows in a realistic model of human nasal/upper airway. *Journal of Aerosol Science, 67*, 188–206.

Ghalati, P. F., Keshavarzian, E., Abouali, O., Faramarzi, A., Tu, J., & Shakibafard, A. (2012). Numerical analysis of micro-and nano-particle deposition in a realistic human upper airway. *Computers in Biology and Medicine, 42*, 39–49.

Hahn, I., Scherer, P. W., & Mozell, M. M. (1993). Velocity profiles measured for airflow through a large-scale model of the human nasal cavity. *Journal of Applied Physiology, 75*, 2273–2287.

Houzeaux, G., Aubry, R., & Vázquez, M. (2011). Extension of fractional step techniques for incompressible flows: The preconditioned orthomin(1) for the pressure schur complement. *Computers & Fluids, 44*, 297–313.

Houzeaux, G., Garcia, M., Cajas, J. C., Artigues, A., Olivares, E., Labarta, J., et al. (2016). Dynamic load balance applied to particle transport in fluids. *International Journal of Computational Fluid Dynamics, 30*, 408–418.

Houzeaux, G., & Principe, J. (2008). A variational subgrid scale model for transient incompressible flows. *IJCFD, 22*, 135–152.

Houzeaux, G., & Vázquez, M., (2008). Parallel implementation of a predictor-corrector scheme for the solution of the navier-stokes Eqs.

Hunt, J., (1987). Vorticity and vortex dynamics in complex turbulent flows. In: *Canadian Society for Mechanical Engineering, Transactions* (ISSN 0315–8977), (pp. 21–35), *vol. 11*, no. 1.

Jayaraju, S. T., Brouns, M., Lacor, C., Belkassem, B., & Verbanck, S. (2008). Large eddy and detached eddy simulations of fluid flow and particle deposition in a human mouth-throat. *Journal of Aerosol Science, 39*, 862–875.

Karypis, G., Metis: Serial graph partitioning and fill-reducing matrix ordering. 1995–2015. Available at: ⟨http://glaros.dtc.umn.edu/gkhome/views/metis⟩.

Kelly, J. T., Asgharian, B., Kimbell, J. S., & Wong, B. A. (2004). Particle deposition in human nasal airway replicas manufactured by different methods. part i: Inertial regime particles. *Aerosol Science and Technology, 38*, 1063–1071.

Kesavan, J., Bascom, R., Laube, B., & Swift, D. L. (2000). The relationship between particle deposition in the anterior nasal passage and nasal passage characteristics. *Journal of Aerosol Medicine, 13*, 17–23.

Kesavanathan, J., Bascom, R., & Swift, D. L. (1998). The effect of nasal passage characteristics on particle deposition. *Journal of Aerosol Medicine, 11*, 27–39.

Kesavanathan, J., & Swift, D. L. (1998). Human nasal passage particle deposition: The effect of particle size, flow rate, and anatomical factors. *Aerosol Science and Technology, 28*, 457–463.

Kolanjiyil, A. V., & Kleinstreuer, C. (2013). Nanoparticle mass transfer from lung airways to systemic regions-part i: Whole-lung aerosol dynamics. *Journal of Biomechanical Engineering, 135*, 121003.

Ligrani, P., & Niver, R. (1988). Flow visualization of dean vortices in a curved channel with 40 to 1 aspect ratio. *The Physics of fluids, 31*, 3605–3617.

Lin, C. L., Tawhai, M. H., McLennan, G., & Hoffman, E. A. (2007). Characteristics of the turbulent laryngeal jet and its effect on airflow in the human intra-thoracic airways. *Respiratory Physiology & Neurobiology, 157*, 295–309.

Rennie, C. E., Gouder, K. A., Taylor, D. J., Tolley, N. S., Schroter, R. C., & Doorly, D. J. (2011). Nasal inspiratory flow: At rest and sniffing. *International Forum of Allergy and Rhinology, 1*, 128–135.

Saksono, P. H., Nithiarasu, P., Sazonov, I., & Yeo, S. Y. (2011). Computational flow studies in a subject-specific human upper airway using a one-equation turbulence model. influence of the nasal cavity. *International Journal for Numerical Methods in Engineering, 87*, 96–114.

Shi, H., Kleinstreuer, C., & Zhang, Z. (2007a). Modeling of inertial particle transport and deposition in human nasal cavities with wall roughness. *Journal of Aerosol Science, 38*, 398–419.

Shi, H., Kleinstreuer, C., & Zhang, Z. (2007b). Modeling of inertial particle transport and deposition in human nasal cavities with wall roughness. *Journal of Aerosol Science, 38*, 398–419.

Shi, H., Kleinstreuer, C., & Zhang, Z. (2008). Dilute suspension flow with nanoparticle deposition in a representative nasal airway model. *Physics of Fluids, 20(1994-present)*, 013301.

Shi, H., Kleinstreuer, C., & Zhang, Z. (2008b). Dilute suspension flow with nanoparticle deposition in a representative nasal airway model. *Physics of Fluids, 20*, 013301.

Sumer, B. M., & Fredsøe, J. (2006). *Hydrodynamics around Cylindrical Strucures. 26*. World Scientific.

Taubin, G., (1995). Curve and surface smoothing without shrinkage. In: *Computer Vision, 1995. Proceedings of the Fifth International Conference on, IEEE*, (pp. 852–857).

Taylor, D. J., Doorly, D. J., & Schroter, R. C. (2010). Inflow boundary profile prescription for numerical simulation of nasal airflow. *Journal of the Royal Society Interface, 7*, 515–527.

Vázquez, M., Houzeaux, G., Koric, S., Artigues, A., Aguado-Sierra, J., Arís, R., et al. (2016). Alya: Multiphysics engineering simulation toward exascale. *Journal of Computational Science, 14*, 15–27.

Wilcox, D. C., et al. (1998). Turbulence modeling for CFD. *DCW industries Louisiana Canada, CA, 2*.

Zhang, Z., & Kleinstreuer, C. (2011). Computational analysis of airflow and nanoparticle deposition in a combined nasalâ€“oralâ€”tracheobronchial airway model. *Journal of Aerosol Science, 42*, 174–194.

Zhao, K., Scherer, P. W., Hajiloo, S. A., & Dalton, P. (2004). Effect of anatomy on human nasal air flow and odorant transport patterns: Implications for olfaction. *Chemical Senses, 29*, 365–379.